A pseudo-transient Newton-Krylov-Schwarz method for incompressible Navier-Stokes equations with slip conditions for bifurcation analysis

Wen-Lieh Hsu and Feng-Nan Hwang[*]

We develop a parallel pseudo-transient Newton-Krylov-Schwarz (Ψ-NKS) algorithm based on the Galerkin/least-squares finite element method for incompressible Navier-Stokes equations with slip boundary conditions. Many research works suggest that the slip condition can produce a more accurate numerical solution of fluid flow motion near the boundary for the case with a rough surface, porous media flows, and non-Newtonian flows. This study aims to investigate numerically how the slip condition affects the physical behavior of the fluid flows by using the Ψ-NKS algorithm, including the flow structure of the lid-driven cavity and the critical Reynolds number for the pitchfork bifurcation of sudden expansion flows.

Keywords and phrases: Incompressible Navier-Stokes equations, slip boundary conditions, domain decomposition method, Newton-Krylov-Schwarz algorithm, pitchfork bifurcation analysis.

1. Introduction

Navier-Stokes equations with the no-slip boundary condition (i.e., the flow velocity at the boundary is equal to the velocity of the solid boundary) are commonly used for the numerical simulation of fluid flows passing through a solid object or confined by walls. For most fluid flows, the no-slip boundary conditions can accurately describe their motions near boundaries, but sometimes the slip phenomena of fluid flows are observed in gas flows, non-Newtonian fluids, and contact motion. In the context of Newtonian liquids instead of the no-slip boundary condition imposed, the slip condition can be used to remove the unphysical singularities, where a moving and stationary wall meet. An alternative approach to resolving the problem is to use the method of molecular dynamics simulation [4]. The slip boundary condition effects were investigated in many pioneer works. For example, in
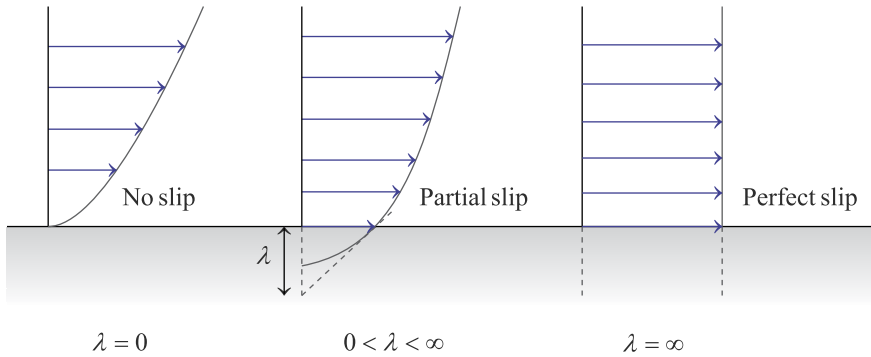
---

[*]Correspondent author.

Figure 1: Interpretation of the slip length λ.

1823, Navier, in his treatise, proposed the concept of slip boundary condition [14]. In 1860, Helmholtz and Piotrowski introduced the term, "coefficient of slip" (Gleitungskoeffizient). In 1875, Kundt and Warburg found that the coefficient of slip was inversely proportional to the pressure by some experiments [12]. Later in 1879, Maxwell derived an expression for the slip [13]. Consider a simple shear flow passing a flat plane. As shown in Figure 1, the slip length, λ, can be interpreted as the distance in the below boundary, where the no-slip boundary condition would be satisfied.

The slip length has been confirmed to be the dependence on some physical properties, such as surface roughness, dissolved gas and bubbles, shear rates, electrical properties, and pressure. The applicability of slip boundary conditions is usually for small-scale systems, including porous media, microfluidics, and biological fluids. In this work, we consider a type of slip boundary condition proposed by John [9, 10], which is given by

$$\boldsymbol{u} \cdot \boldsymbol{n} + \alpha \boldsymbol{n}^T \boldsymbol{\sigma} \boldsymbol{n} = 0 \tag{1}$$

$$\boldsymbol{u} \cdot \boldsymbol{\tau} + \beta^{-1} \boldsymbol{n}^T \boldsymbol{\sigma} \boldsymbol{\tau} = 0 \tag{2}$$

where $\boldsymbol{n}$ is the normal vector to the surface, $\boldsymbol{\tau}$ denotes the tangent vector to the surface, α is the penetration parameter, and $\beta > 0$ is the friction parameter. Besides, $\boldsymbol{\sigma}$ is the Cauchy stress tensor that is defined as

$$\boldsymbol{\sigma} = -pI + 2\mu \mathbb{D}(\boldsymbol{u}),$$

where p is the pressure and the unit tensor is denoted by I, and the velocity deformation tensor is denoted by

$$\mathbb{D}(\boldsymbol{u}) = \frac{\nabla \boldsymbol{u} + \nabla \boldsymbol{u}^T}{2}$$

For simplicity, we do not consider the penetration case, i.e., $\alpha = 0$, hence (1) is reduced to $\boldsymbol{u} \cdot \boldsymbol{n} = 0$.

In the next section, we state the Navier-Stokes (NS) equations and the associated boundary conditions, including the slip-type boundary condition. We also derive the variational formulation of Navier-Stokes equations, which serves as a basis for finite element methods and then discretize the fluid flow equations by using the Galerkin/least-squares (GLS) finite element method. In Section 3, we describe the pseudo-transient Newton-Krylov-Schwarz (Ψ-NKS) algorithm based on the GLS finite element formulation of the NS equations. Pseudo-transient algorithms belong to a class of the continuation methods that are used to find a steady-state solution as well as for the symmetry-breaking analysis [7]. In Section 4, we first validate our fluid flow code and then employ our code to two benchmark problems – the lid-driven cavity problem and the sudden expansion flow problem. We will report on a numerical investigation to show how the slip condition affects the physical behavior of the fluid flows, including the flow structure of the lid-driven cavity and the critical Reynolds number for the pitchfork bifurcation of sudden expansion flows.

2. Incompressible NS equations with slip boundary condition and their variational formulation

Let Ω in $\mathbb{R}^2$ be a bounded computational domain with boundary $\Gamma = \Gamma_{\mathrm{D}} \cup \Gamma_{\mathrm{N}} \cup \Gamma_{\mathrm{sf}}$. Here, we consider three types of boundary conditions, including the Dirichlet-type boundary condition on Γ_{D}, the Neumann-type boundary condition on Γ_{N}, and the slip-with-friction (sf)-type boundary condition on Γ_{sf} [9, 10]. Each pair of any two boundary segments is assumed to be mutually disjoint. The 2D unsteady incompressible Navier-Stokes (NS) equations are given as follows.

(3)
$$\begin{cases} \rho(\partial_t \boldsymbol{u} + \boldsymbol{u} \cdot \nabla \boldsymbol{u}) - \nabla \cdot \boldsymbol{\sigma} = \boldsymbol{f} & \text{in } \Omega \times (0, T] \\ \nabla \cdot \boldsymbol{u} = 0 & \text{in } \Omega \times (0, T] \\ \boldsymbol{u} = \boldsymbol{g} & \text{on } \Gamma_{\mathrm{D}} \times (0, T] \\ \boldsymbol{n} \cdot \boldsymbol{\sigma} = \boldsymbol{h} & \text{on } \Gamma_{\mathrm{N}} \times (0, T] \\ \boldsymbol{u} \cdot \boldsymbol{n} = 0 & \text{on } \Gamma_{\mathrm{sf}} \times (0, T] \\ \boldsymbol{u} \cdot \boldsymbol{\tau} + \beta^{-1} \boldsymbol{n} \cdot \boldsymbol{\sigma}\boldsymbol{\tau} = 0 & \text{on } \Gamma_{\mathrm{sf}} \times (0, T] \\ \boldsymbol{u}|_{t=0} = \boldsymbol{u}_0 & \text{in } \Omega \end{cases}$$

where $\boldsymbol{u} = (u_1, u_2)^T$ is the velocity, ρ is the fluid density, $\boldsymbol{g}$ is the boundary function, $\boldsymbol{n}$ and $\boldsymbol{\tau}$ is the outward normal and tangential vectors to the

boundary Γ, respectively, and $\boldsymbol{u}_0$ is a given initial condition. For the simplicity of the presentation, $\boldsymbol{h}$ is set to be zero. To derive the variational formulation of the NS equations, we first introduce some notations. Let

$$
\begin{aligned}
V_{\boldsymbol{g}} &:= \{\boldsymbol{v} \in (H^1(\Omega))^2 : \boldsymbol{v}|_{\Gamma_\mathrm{D}} = \boldsymbol{g}\}, \\
V_{\boldsymbol{0}} &:= \{\boldsymbol{v} \in (H^1(\Omega))^2 : \boldsymbol{v}|_{\Gamma_\mathrm{D}} = \boldsymbol{0}\}, \\
Q &:= L^2(\Omega)
\end{aligned}
$$

where

$$
\begin{aligned}
L^2(\Omega) &= \{u | u \text{ is defined on } \Omega \text{ and } \int_\Omega u^2 \, dx < \infty\} \\
H^1(\Omega) &= \{u | u \text{ and } \frac{\partial u}{\partial x_i}, i = 1, 2 \text{ belong to } L^2(\Omega)\}
\end{aligned}
$$

Multiplying first equation of (3) both sides by a pair of the test functions $(\boldsymbol{v}, q) \in V_0 \times Q$ and integrating over the domain Ω to obtain

$$
(4) \quad (\rho \partial_t \boldsymbol{u}, \boldsymbol{v}) - (2\mu \nabla \cdot \mathbb{D}(\boldsymbol{u}), \boldsymbol{v}) + (\rho(\boldsymbol{u} \cdot \nabla)\boldsymbol{u}, \boldsymbol{v}) + (\nabla p, \boldsymbol{v}) = (\boldsymbol{f}, \boldsymbol{v})
$$

$$
(5) \quad (\nabla \cdot \boldsymbol{v}, q) = 0
$$

where the inner product $(\cdot, \cdot)$ is defined in $\left(L^2(\Omega)\right)^2$. Next, we apply the integration-by-parts to the diffusion and the pressure terms, respectively.

1. Diffusion term:

$$
\begin{aligned}
(-2\mu \nabla \cdot \mathbb{D}(\boldsymbol{u}), \boldsymbol{v}) &= -2\mu(\nabla \cdot \mathbb{D}(\boldsymbol{u}), \boldsymbol{v}) \\
&= -2\mu \left[\int_\Gamma \mathbb{D}(\boldsymbol{u})\boldsymbol{n} \cdot \boldsymbol{v} \, ds - (\mathbb{D}(\boldsymbol{u}), \nabla \boldsymbol{v}) \right] \\
&= -2\mu \left[\int_\Gamma \mathbb{D}(\boldsymbol{u})\boldsymbol{n} \cdot \boldsymbol{v} \, ds - (\mathbb{D}(\boldsymbol{u}), \mathbb{D}(\boldsymbol{v})) \right]
\end{aligned}
$$

Here, the last equality is held due to

$$
\begin{aligned}
(\mathbb{D}(\boldsymbol{u}), \nabla \boldsymbol{v}) &= \left(\mathbb{D}(\boldsymbol{u}), \frac{\nabla \boldsymbol{v}}{2} \right) + \left(\mathbb{D}(\boldsymbol{u})^T, \frac{\nabla \boldsymbol{v}^T}{2} \right) \\
&= \left(\mathbb{D}(\boldsymbol{u}), \frac{\nabla \boldsymbol{v}}{2} \right) + \left(\mathbb{D}(\boldsymbol{u}), \frac{\nabla \boldsymbol{v}^T}{2} \right) = (\mathbb{D}(\boldsymbol{u}), \mathbb{D}(\boldsymbol{v}))
\end{aligned}
$$

2. Pressure term:

$$
(\nabla p, \boldsymbol{v}) = \int_\Gamma p(\boldsymbol{n} \cdot \boldsymbol{v}) \, ds - (p, \nabla \cdot \boldsymbol{v})
$$

Then the left hand side of Eq. (4) is written as

$$- 2\mu \left[\int_{\Gamma} \mathbb{D}(\boldsymbol{u})\boldsymbol{n} \cdot \boldsymbol{v}\, ds - (\mathbb{D}(\boldsymbol{u}), \mathbb{D}(\boldsymbol{v})) \right] + \rho((\boldsymbol{u} \cdot \nabla)\boldsymbol{u}, \boldsymbol{v})$$

$$+ \int_{\Gamma} p(\boldsymbol{n} \cdot \boldsymbol{v})\, ds - (p, \nabla \cdot \boldsymbol{v})$$

$$\Rightarrow 2\mu(\mathbb{D}(\boldsymbol{u}), \mathbb{D}(\boldsymbol{v})) + \rho((\boldsymbol{u} \cdot \nabla)\boldsymbol{u}, \boldsymbol{v}) - (p, \nabla \cdot \boldsymbol{v}) - 2\mu \int_{\Gamma} \mathbb{D}(\boldsymbol{u})\boldsymbol{n} \cdot \boldsymbol{v}\, ds$$

$$+ \int_{\Gamma} p(\boldsymbol{n} \cdot \boldsymbol{v})\, ds$$

$$\Rightarrow 2\mu(\mathbb{D}(\boldsymbol{u}), \mathbb{D}(\boldsymbol{v})) + \rho((\boldsymbol{u} \cdot \nabla)\boldsymbol{u}, \boldsymbol{v}) - (p, \nabla \cdot \boldsymbol{v}) - \int_{\Gamma} (2\mu\mathbb{D}(\boldsymbol{u}) - pI)\boldsymbol{n} \cdot \boldsymbol{v}\, ds$$

and we can decompose the boundary into the three types

$$\int_{\Gamma} (2\mu\mathbb{D}(\boldsymbol{u}) - pI)\boldsymbol{n} \cdot \boldsymbol{v}\, ds$$

$$= \int_{\Gamma_{\mathrm{D}}} (2\mu\mathbb{D}(\boldsymbol{u}) - pI)\boldsymbol{n} \cdot \boldsymbol{v}\, ds + \int_{\Gamma_{\mathrm{N}}} (2\mu\mathbb{D}(\boldsymbol{u}) - pI)\boldsymbol{n} \cdot \boldsymbol{v}\, ds$$

$$+ \int_{\Gamma_{\mathrm{sf}}} (2\mu\mathbb{D}(\boldsymbol{u}) - pI)\boldsymbol{n} \cdot \boldsymbol{v}\, ds$$

Here, the first two terms are vanished, since $\boldsymbol{v} = 0$ on Γ_D and $\boldsymbol{\sigma} \cdot \boldsymbol{n} = 0$ on Γ_N. For the last term involving the slip boundary condition, we can decompose the test function $\boldsymbol{v}$ on Γ_{sf} into two orthonormal components, that is

$$\boldsymbol{v} = (\boldsymbol{v} \cdot \boldsymbol{n})\boldsymbol{n} + (\boldsymbol{v} \cdot \boldsymbol{\tau})\boldsymbol{\tau}$$

Then the line integral on Γ_{sf} becomes

$$\int_{\Gamma_{\mathrm{sf}}} (2\mu\mathbb{D}(\boldsymbol{u}) - pI)\boldsymbol{n} \cdot \boldsymbol{v}\, ds$$

$$= \int_{\Gamma_{\mathrm{sf}}} \boldsymbol{n}^T(2\mu\mathbb{D}(\boldsymbol{u}) - pI)\boldsymbol{n}\boldsymbol{v} \cdot \boldsymbol{n}\, ds + \int_{\Gamma_{\mathrm{sf}}} \boldsymbol{n}^T(2\mu\mathbb{D}(\boldsymbol{u}) - pI)\boldsymbol{\tau}\boldsymbol{v} \cdot \boldsymbol{\tau}\, ds$$

$$= - \int_{\Gamma_{\mathrm{sf}}} \beta(\boldsymbol{u} \cdot \boldsymbol{\tau})(\boldsymbol{v} \cdot \boldsymbol{\tau})\, ds$$

since the slip boundary condition $\boldsymbol{v} \cdot \boldsymbol{n} = 0$ and $\boldsymbol{n} \cdot \boldsymbol{\sigma\tau} = -\beta(\boldsymbol{u} \cdot \boldsymbol{\tau})$. In summary, the variational formulation of NS equations with the slip boundary

condition can be stated as. Find $(\boldsymbol{u}, p) \in (V_{\boldsymbol{g}}, Q)$ such that

(6) $$B(\boldsymbol{u}, p; \boldsymbol{v}, q) = (\boldsymbol{f}, \boldsymbol{v}) \quad \forall(\boldsymbol{v}, q) \in (V_{\boldsymbol{0}}, Q)$$

with

$$\begin{aligned} B(\boldsymbol{u}, p; \boldsymbol{v}, q) &= (\rho\partial_t\boldsymbol{u}, \boldsymbol{v}) + 2\nu(\mathbb{D}(\boldsymbol{u}), \mathbb{D}(\boldsymbol{v})) + ((\boldsymbol{u} \cdot \nabla)\boldsymbol{u}, \boldsymbol{v}) - (\nabla \cdot \boldsymbol{v}, p) \\ &\quad - (\nabla \cdot \boldsymbol{u}, q) + \int_{\Gamma_{\mathrm{sf}}} \beta(\boldsymbol{u} \cdot \boldsymbol{\tau})(\boldsymbol{v} \cdot \boldsymbol{\tau}) \, ds \end{aligned}$$

3. Solution algorithm

To discretize the NS equations (6), we use different methods for time and space domains. In the time domain, we use implicit backward Euler's finite difference method and in the space domain, we use P_1-P_1 (continuous linear element for both velocity and pressure) stabilized Galerkin/least-square (GLS) finite element method on a given triangular mesh, $\mathcal{T}^h = \{K\}$.

3.1. Galerkin/least-square finite element formulation

Let n be the time step number such that $t_n = (\delta t_n)n$. For the stabilized GLS finite element method, the variational formulation of the time-dependent NS equations take the form as Find $\boldsymbol{u}_h^{(n+1)} \in V_g^h$ and $p_h^{(n+1)} \in P^h$ such that

$$B(\boldsymbol{u}_h^{(n+1)}, p_h^{(n+1)}; \boldsymbol{v}, q) = (\boldsymbol{f}, \boldsymbol{v}) \quad \forall(\boldsymbol{v}, q) \in V_0^h \times P^h$$

with

$$\begin{aligned} &B(\boldsymbol{u}^{(n+1)}, p^{(n+1)}; \boldsymbol{v}, q) \\ &= \left(\rho\left(\frac{\boldsymbol{u} - \boldsymbol{u}^{(n)}}{\delta t_n}\right), \boldsymbol{v} \right) + ((\rho\nabla\boldsymbol{u}) \cdot \boldsymbol{u}, \boldsymbol{v}) + (\mu\nabla\boldsymbol{u}, \nabla\boldsymbol{v}) - (\nabla \cdot \boldsymbol{v}, p) \\ &\quad - (\nabla \cdot \boldsymbol{u}, q) + \int_{\Gamma_{\mathrm{sf}}} \beta(\boldsymbol{u} \cdot \boldsymbol{\tau})(\boldsymbol{v} \cdot \boldsymbol{\tau}) \, ds \\ &\quad + \sum_{K \in \mathcal{T}^h} \left(\rho\left(\frac{\boldsymbol{u} - \boldsymbol{u}^{(n)}}{\delta t_n}\right) + (\nabla\boldsymbol{u}) \cdot \boldsymbol{u} + \nabla p - \boldsymbol{f}, \tau\big((\nabla\boldsymbol{v}) \cdot \boldsymbol{v} + \nabla q\big) \right)_K \\ &\quad + (\nabla \cdot \boldsymbol{u}, \delta\nabla \cdot \boldsymbol{v})_K \end{aligned}$$

where $\boldsymbol{u}^{(n)}$ is the velocity at the current time step, and $\boldsymbol{u}$ and $\boldsymbol{p}$ are unknown velocity and pressure, respectively, at the next time step. In the variational

formulation of GLS method, the stabilization parameters τ and δ we used are suggested by Franca and Frey [5].

$$\tau(\boldsymbol{x}, Re_K(\boldsymbol{x})) = \frac{h_K}{2\|\boldsymbol{u}(\boldsymbol{x})\|_2}\xi(Re_K(\boldsymbol{x}))$$
$$\delta(\boldsymbol{x}, Re_K(\boldsymbol{x})) = \|\boldsymbol{u}(\boldsymbol{x})\|_2 h_K \xi(Re_K(\boldsymbol{x}))$$

Here, Re_K is an element Reynolds number defined as follows:

$$Re_K(\boldsymbol{x}) = \frac{\rho|\boldsymbol{u}(\boldsymbol{x})|_2 h_K}{12\mu}$$

and the function ξ is defined as

$$\xi(Re_K(\boldsymbol{x})) = \begin{cases} Re_K(\boldsymbol{x}), & 0 \le Re_K(\boldsymbol{x}) \le 1 \\ 1, & Re_K(\boldsymbol{x}) \ge 1 \end{cases}$$

which distinguishes the locally convection-dominated flow as $Re_K(\boldsymbol{x}) \ge 1$ and the locally diffusion-dominated flow as $0 \le Re_K(\boldsymbol{x}) \le 1$.

3.2. Pseudo-transient Newton-Krylov-Schwarz algorithm

The ΨNKS algorithm [7] can be described as follows. Suppose s_n is an approximate solution at the current time step t_n. At each time step, we solve the following large, sparse, nonlinear algebraic system of equations by using the Newton-Krylov-Schwarz algorithm for finding new approximation, s_{n+1} at t_{n+1}.

$$G_{n+1}(s) \equiv B(x)\frac{s - s_n}{\delta t_n} + D(s, Re)x - F(s) = 0,$$

where

$$B = \begin{bmatrix} M + M_\epsilon^w & 0 \\ M_\epsilon^q & 0 \end{bmatrix}, \quad \mathbf{s} = \begin{bmatrix} \mathbf{v} \\ p \end{bmatrix},$$
$$D(\mathbf{s}, Re) = \begin{bmatrix} K + K_\epsilon^w + C(\mathbf{v}, Re) + C_\epsilon^w(\mathbf{v}, Re) & G + G_\epsilon^w \\ G^T + K_\epsilon^q + C_\epsilon^q(\mathbf{v}, Re) & G_\epsilon^q \end{bmatrix}.$$

$\mathbf{v} \in \mathbb{R}^n$ and $\mathbf{p} \in \mathbb{R}^m$ are the vectors of unknown nodal values of the velocity $\mathbf{v}_h \in V_g^h$ and pressure $p_h \in P^h$, respectively. The matrices M, K, C, and G are derived from the time-dependent, diffusive, convective, and pressure

terms, respectively. The vector F corresponds to the slip boundary condition. The terms with the subscript ϵ represent the stabilization terms. The Reynolds number is defined as $Re = \dfrac{\rho U L}{\mu}$, where ρ is the density of the fluid, U is the characteristic velocity, L is the characteristic length, and μ is the dynamic viscosity of the fluid. Then new approximation $\mathbf{s}_{n+1}$ at next time step t_{n+1} can be obtained via the following procedure:

- **Step 0:** Set $k = 0$ and $\mathbf{x}^{(0)} = \mathbf{s}_n$ and evaluate $g_0 = \|G_{n+1}(\mathbf{x}^{(0)})\|_2$
- **Step 1**: Evaluate the Jacobian matrix, $G'_{n+1}(\mathbf{x}^{(k)})$.
- **Step 2:** Find a Newton direction $\Delta \mathbf{y}^{(k)}$ by solving approximately the preconditioned Jacobian system,

$$G'_{n+1}(\mathbf{x}^{(k)})\Delta \mathbf{x}^{(k)} = -G_{n+1}(\mathbf{x}^{(k)})$$

  for $\Delta \mathbf{x}^{(k)}$ by a Krylov subspace method, such as Generalized minimal residual method (GMRES) [15] with an additive Schwarz preconditioner M_k^{-1} [7].
- **Step 3:** Obtain the new approximation $\mathbf{x}^{(k+1)} = \mathbf{x}^{(k)} + \lambda^{(k)}\Delta \mathbf{x}^{(k)}$, where $\lambda^{(k)} \in (0, 1]$ is a damping parameter.
- **Step 4:** Check if $\|G(\mathbf{x}^{(k+1)})\|_2 < rtol \cdot g_0$ or $\|G(\mathbf{x}^{(k+1)})\|_2 < atol$ then set $\mathbf{s}_{n+1} = \mathbf{x}^{(k+1)}$ and update δt_{n+1} else $k = k + 1$ go to **Step 1**.

Note that δt_n is conveniently chosen as a fixed constant value, which is known as the Rosenbrock method. However, it is more efficient to employ the strategy for timestep selection based on the norm of the step $\|\mathbf{s}_{n+1} - \mathbf{s}_n\|_2$, which is given by $\delta t_{n+1} = \phi(\delta t_n \|\mathbf{s}_{n+1} - \mathbf{s}_n\|^{-1})$. Here, ϕ satisfies the condition

$$\phi(\xi) = \begin{cases} \xi, & \xi \leq \delta t_{max} \\ \delta t_{max}, & \xi \geq \delta t_{max} \end{cases}$$

where δt_{max} is an upper bound for the timesteps $\{\delta t_n\}$.

4. Numerical results and discussions

Our parallel fluid solver was implemented on the top of the Portable, Extensible Toolkit for Scientific computation (PETSc) package [3]. In addition, the parallel fluid solver is integrated with other pre-processing and post-processing software packages, including: (1) the geometry and mesh generation toolkit, CUBIT [2]; (2) the mesh partitioner, ParMetis, for the purpose of parallel processing [11]; (3) the multi-platform data analysis and
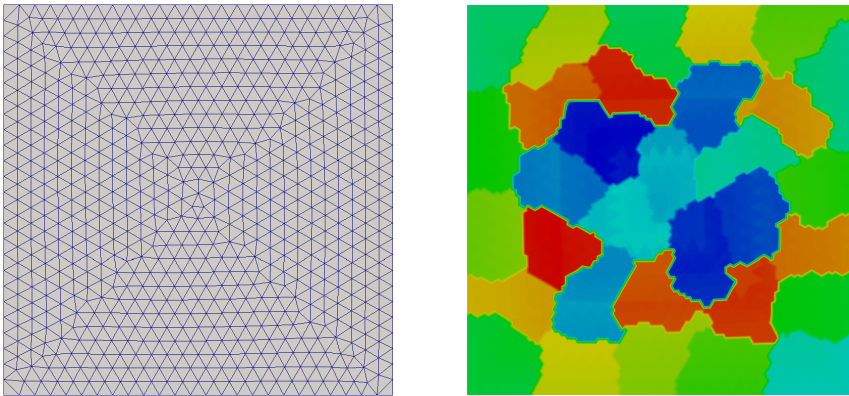
Figure 2: A sample mesh (left) and a sample partition (right) with $np = 32$.

visualization application, ParaView, which is used to plot the pressure contours, streamlines, and velocity profiles for data analysis [1]. All numerical simulations were performed on a PC of clusters.

4.1. Code validation

The test example for our parallel code validation is taken from [6] with some modification so that it can be used for checking the steady-state flow case. The forcing term,

$$\boldsymbol{f} = \left(\begin{array}{c} \dfrac{2\nu}{l_s^2} \sin \dfrac{x}{l_s} \cos \dfrac{y}{l_s} \\ -\dfrac{2\nu}{l_s^2} \cos \dfrac{x}{l_s} \sin \dfrac{y}{l_s} \end{array} \right)$$

is determined when the exact solution of $\boldsymbol{u}$ and p takes the form of

$$\boldsymbol{u} = \left(\begin{array}{c} \sin \dfrac{x}{l_s} \cos \dfrac{y}{l_s} \\ -\cos \dfrac{x}{l_s} \sin \dfrac{y}{l_s} \end{array} \right), \quad p = \dfrac{1}{4} \left(\cos \dfrac{2x}{l_s} + \cos \dfrac{2y}{l_s} \right)$$

defined on the domain $\Omega = [0, \pi]^2 \in \mathbb{R}^2$. Figure 2 displays a sample mesh and a sample partition with the number of subdomains, $np = 32$, for defining the Schwarz-type preconditioner.

At the beginning, we assume $\boldsymbol{f} = 0$ at $t = 0$. We set Reynolds number $Re = \dfrac{\pi}{\nu} = 5$ (or $\nu = \dfrac{\pi}{5}$) and the slip length $l_s = 0.5(= \dfrac{1}{\beta})$. Table 1 lists

the mesh information for a sequence of uniformly refined triangular meshes used for the numerical experiment. The initial time step size is set to be 10.

Table 1: A sequence of uniformly refined triangular meshes

Meshes	h_K	# of elements	# of nodes	# of unknowns
Mesh A	0.127549	1,400	751	2,253
Mesh B	0.0637745	5,600	2,901	8,703
Mesh C	0.03188725	22,400	11,401	34,203
Mesh D	0.015943625	89,600	45,201	135,603
Mesh E	0.007971813	358,400	180,001	540,003

To validate the ΨNKS algorithm, we summarize its convergence history by using different mesh sizes at each time step in Table 2. The result shows

Table 2: The history of the nonlinear residual norm for ΨNKS method

Meshes	Mesh A	Mesh B	Mesh C	Mesh D	Mesh E
Time step #	Nonlinear Residual norm, $\|G(x)\|_2$.				
0	0.00E+00	0.00E+00	0.00E+00	0.00E+00	0.00E+00
1	6.92E-04	1.83E-04	3.75E-05	7.00E-06	1.27E-06
2	6.29E-06	8.30E-07	1.23E-07	1.69E-08	2.22E-09
3	8.14E-10	8.30E-07	1.23E-07	1.69E-08	2.22E-09
4	8.14E-10	8.30E-07	1.23E-07	1.69E-08	2.22E-09

that the ΨNKS algorithm is quite efficient for finding the steady-state solution, requiring only a few iterations. We then perform the grid convergence test by plotting the horizontal velocity profiles along $x = \pi/4$ and the vertical velocity profile along $y = \pi/4$, respectively. As shown in Figure 3, all the curves obtained using different mesh sizes nearly coincide, but if we zoom in on the middle part of the plots (See Figure 4), we can still tell the differences between the five curves. Finer meshes, such as Mesh D or Mesh E, are needed to obtain the grid-independent results. Next, the comparison plots, including the pressure contours, the streamlines, the u_1- and u_2-components of the velocity field for the computed solution and the exact solutions are shown in Figure 5. They are almost indistinguishable.

4.2. Applications

In this section, we present the numerical results for simulating two benchmark problems – the lid-driven cavity problem and the sudden expansion problem, but now some slip boundary conditions are imposed on the walls, which are not commonly considered in the literature.
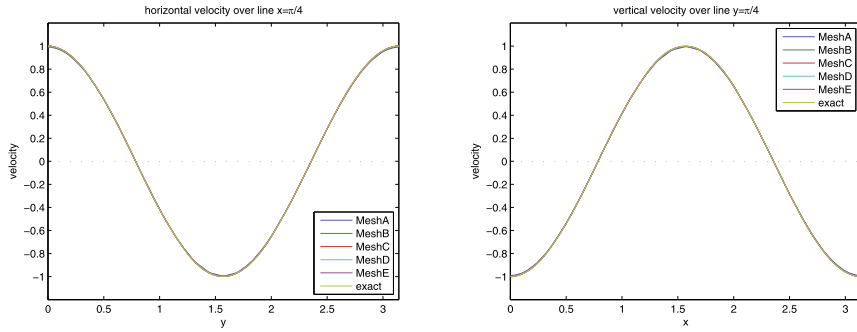
Figure 3: The u_1- (left) and u_2- (right) components of the velocity profiles along the line $x = \frac{\pi}{4}$ and $y = \frac{\pi}{4}$, respectively.
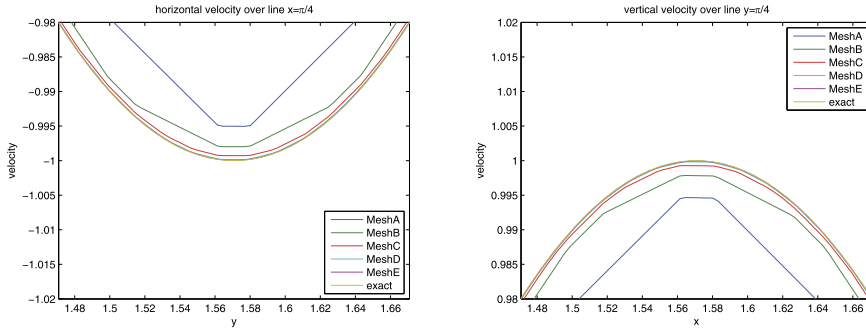

Figure 4: The u_1- (left) and u_2- (right) components of the zoom-in velocity profiles along the line $x = \frac{\pi}{4}$ and $y = \frac{\pi}{4}$, respectively.

4.2.1. Lid-driven cavity flows. The classical cavity we consider has three stationary sides and one moving side with tangential velocity to the side, and the flow is driven by the tangential motion of a single side [8]. In this case, we set the computational domain in a unit square domain, $[0, 1] \times [0, 1] \subset \mathbb{R}^2$. Since the boundaries are orthogonal to the coordinates system, we impose different types of boundary conditions on the boundaries. Figure 6 shows the geometry configuration of the lid-driven cavity problem. The Dirichlet-type boundary condition is imposed on the top wall, i.e., $u_1 = 1$ and $u_2 = 0$. The slip-type boundary condition is set on the three other walls. The Reynolds number, Re, is based on the velocity of the moving wall as the characteristic velocity and the length of the boundary as the characteristic length. The typical steady-flow patterns in the two-dimensional
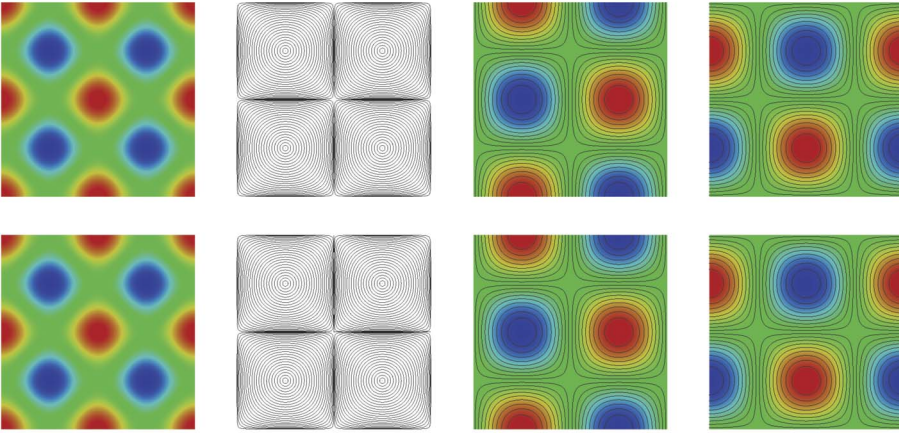
Figure 5: A comparison of the exact solution (top row) and the computed solution (bottom row). From left to right: (a) pressure contours, (b) streamlines, (c) the u_1-component and (d) the u_2-component of the velocity field.
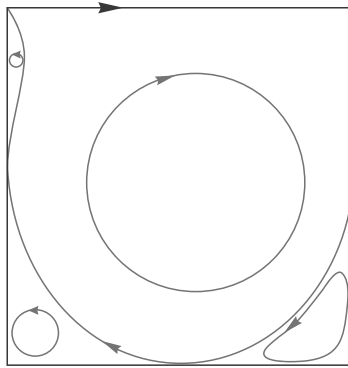

Figure 6: The geometry configuration of the lid-driven cavity problem.

square cavity are as follows: one primary eddy and three secondary eddies near the corners. The results presented in this section are obtained by using Mesh E. We consider the steady-state cavity flows at $Re = 1000$. The streamline plots obtained by the ΦNKS algorithm are presented in Figure 7 for the different values of the slip parameter, $\beta = 0.0, 0.01, 0.05, 0.1, 0.5$ and 1.0. As shown in this figure, the flow patterns for each case are quite similar. The major difference is that compared to the case of the no-slip condition, i.e., $\beta = 0.0$, one additional eddy is formed near the left bottom of the cavity
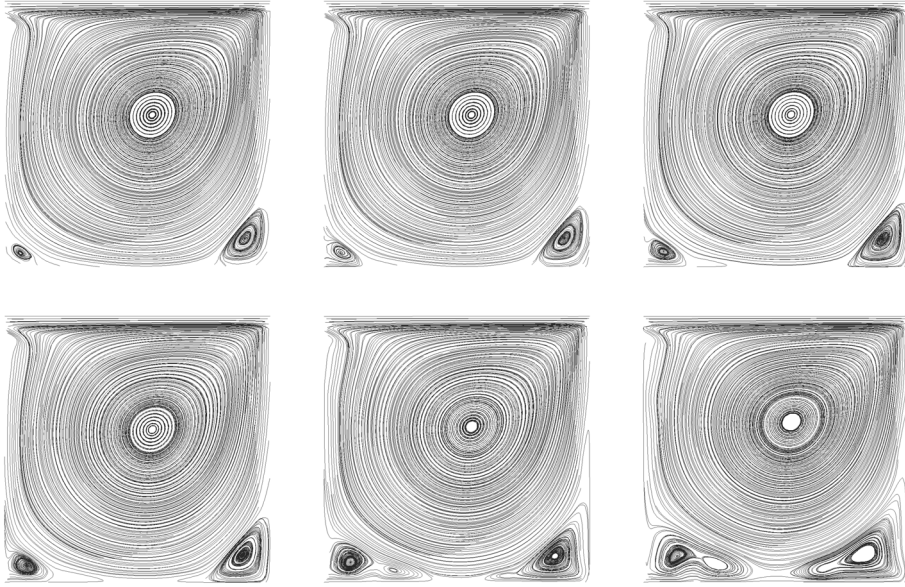
Figure 7: Steady-state case. The streamline profiles with different slip parameters, $\beta = 0.0, 0.01$, and 0.05 (top row) and $\beta = 0.1, 0.5$, and 1.0 (bottom row) for $Re = 1000$.

for $\beta = 0.5$ and 1.0 cases. Hence, we may conclude that the slip boundary condition has some impact on the behavior of flows near the boundary. We summarize the position of the center of the primary eddy with different slip parameters, β, in Table 3 for $Re = 200$. Since the diameter of the mesh is $h_K \approx 0.002$, the difference for the center position of the primary eddy could be ignored. Hence, we can infer that the slip boundary condition does not significantly change the global flow pattern but only does so locally.

4.3. Sudden expansion flows

The sudden expansion flows come from a long channel of height $2d$, which suddenly expands symmetrically with right angles to a long channel of height D, where $D > 2d$, the expansion ratio **ER** is defined as the ratio of the downstream channel height D to the upstream channel height $2d$, i.e., $\mathbf{ER} = \dfrac{D}{2d}$, and the Reynolds number here is defined as $Re = \dfrac{Ud}{\nu}$ based on the maximum inlet velocity U, the half-height of the upstream channel d and the kinematic viscosity ν. The schematic diagram of the sudden expansion model

Table 3: The time-dependent lid-driven cavity problem. The position of the center of the primary eddy with different slip parameter β. Here, D_x is the distance between two primary eddies for the no slip and slip cases

β	x	y	D_x
0.0	0.604279	0.668229	–
0.01	0.604257	0.668247	0.000029
0.05	0.604167	0.668313	0.000140
0.1	0.604058	0.668395	0.000276
0.5	0.603175	0.669043	0.001372
1.0	0.602070	0.669842	0.002735
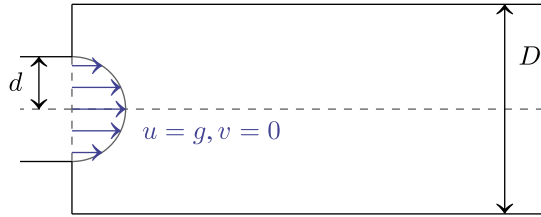
Figure 8: The schematic diagram of sudden expansion model.

is shown in Figure 8. The Dirichlet-type boundary condition is imposed on the left inflow boundary and on the left wall. The slip-type boundary condition is set on both of the top and bottom walls.

In our simulations, we only consider the downstream channel in the computational domain, which we set with height $D = 6$ and long $L = 40$. Since the computational domain is long enough, the flows can achieve fully developed. For easily to set different expansion ratios **ER**, we use half of the upstream channel height $d = \dfrac{D}{2\mathbf{ER}}$ to set up the inflow function. The horizontal velocity of inflow we defined as a parabolic function such as

$$u = \begin{cases} -\dfrac{1}{d}\dfrac{(y-d)(y+d)}{d^2}, & \text{if} \quad -d \le y \le d \\ 0, & \text{otherwise} \end{cases}$$

and the vertical velocity of inflow is defined as $v = 0$, for all y. The grid information is provided in Table 4. A sample mesh and a sample partition with $np = 32$ are shown in Figure 9.

The pitchfork bifurcation is a basic phenomenon, and it occurs in a system with symmetry property. There are two types of pitchfork bifurcation: supercritical pitchfork bifurcation and subcritical pitchfork bifurcation. In

Table 4: The information of channel grids

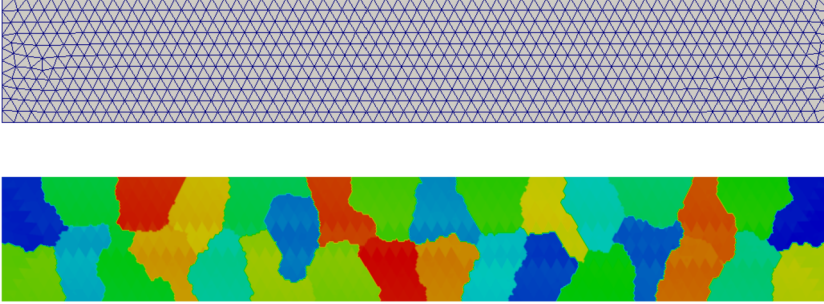| Meshes	h_K	# of elements	# of nodes	# of unknowns
MeshA_SE	0.6	1,460	808	2,424
MeshB_SE	0.3	5,840	3,075	9,225
MeshC_SE	0.15	23,360	11,989	35,967
MeshD_SE	0.075	93,440	47,337	142,011

Figure 9: A sample mesh (top) and a sample partition (bottom) with $np = 32$.

our works, we only consider the supercritical one, which often appears in symmetric channel flows. For sudden expansion flows, the pitchfork bifurcation becomes obviously after some critical Reynolds number Re_c. As follows, we investigate numerically how the effect of the slip boundary condition on the pitchfork bifurcation happened in the sudden expansion flows. Here, we introduce a time-dependent perturbation into the inlet velocity, which was modified to have a time-periodic behavior for three cycles; after that, it was held at its original value. The shift perturbation is defined for $0 < t < 45$ as:

- **Shift up perturbation**

$$u = \begin{cases} -\dfrac{1}{d}(1 + 0.2|\sin\frac{\pi t}{15}|)\dfrac{(y+d)(y-d-0.2)}{(d+0.1)^2}, & \text{if} \quad -d \leq y \leq 0.1 \\ -\dfrac{1}{d}(1 + 0.2|\sin\frac{\pi t}{15}|)\dfrac{(y+d-0.2)(y-d)}{(d-0.1)^2}, & \text{if} \quad 0.1 \leq y \leq d \end{cases}$$

- **Shift down perturbation**

$$u = \begin{cases} -\dfrac{1}{d}(1 + 0.2|\sin\frac{\pi t}{15}|)\dfrac{(y+d)(y-d+0.2)}{(d-0.1)^2}, & \text{if} \quad -d \leq y \leq -0.1 \\ -\dfrac{1}{d}(1 + 0.2|\sin\frac{\pi t}{15}|)\dfrac{(y+d+0.2)(y-d)}{(d+0.1)^2}, & \text{if} \quad -0.1 \leq y \leq d \end{cases}$$
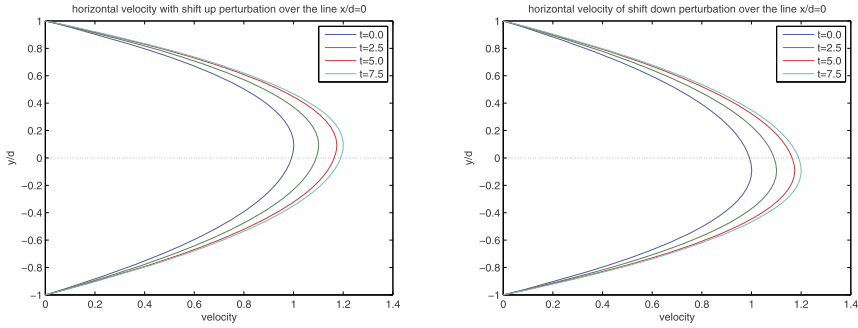
Figure 10: The shifted up (left) and the shifted down (right) profiles of inflow periodic perturbations for half cycle.
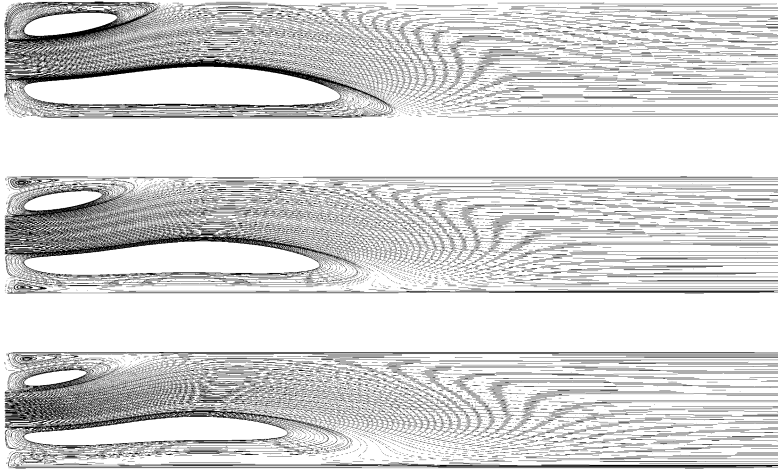

Figure 11: The streamlines at $Re = 60$ with shifted-up perturbation for $\beta = 0$ (top), 0.5 (middle), and 1.0 (bottom).

The shifted perturbation profiles of periodic inflow perturbations for half of the first cycle are shown in Figure 10. We can see that the maximum horizontal velocity of periodic perturbations is shifted up and down with $y/d = 0.1$.

Figures 11 and 12 show the simulated results for slip parameter $\beta = 0.5$ and 1.0 compared to the no-slip cases, with the shifted-up and shifted-down perturbations. Observed from these sets of figures, we find that the varied slip parameter makes the flow patterns significantly different from the no-slip case. Recall that the reattachment point is defined as a posi-
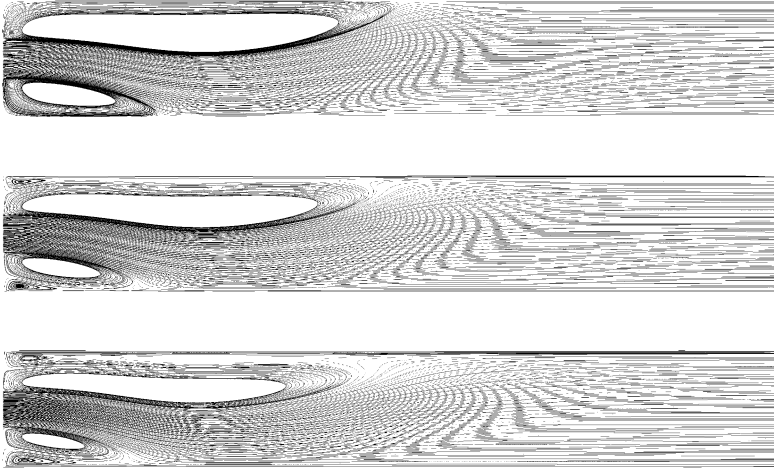
Figure 12: The streamlines at $Re = 60$ with the shifted-down perturbation for $\beta = 0$ (top), 0.5 (middle), and 1.0 (bottom).
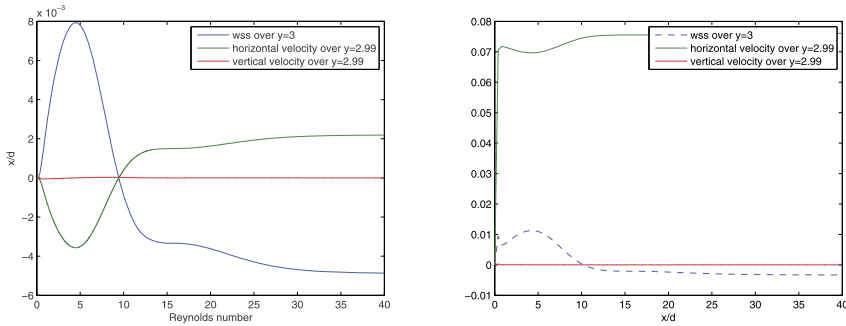

Figure 13: The data near the upper boundary of **ER** $= 3$ of Reynolds number $Re = 45$ with $\beta = 0.0$ (left) and $\beta = 0.5$ (right).

tion where both of the horizontal and vertical velocities are zero near the boundary. We notice that there is no reattachment point found within the channel for the cases of $\beta = 0.5$ and 1.0. Instead of using the difference between two reattachment points on the upper and lower walls, the sign change of the wall shear stress (WSS) (as shown in Figure 13) could be a good option for studying pitchfork bifurcations for slip boundary condition cases.

In the following, we investigate how the expansion ratio **ER** affects the bifurcation phenomenon. Figures 14–16 show the bifurcation diagrams for
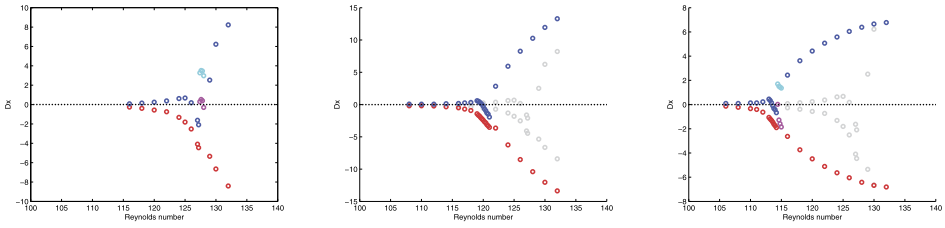
Figure 14: The bifurcation diagram of the sudden expansion flow problem for **ER** $= 2$ with $\beta = 0.0$ (left), 0.5 (middle), and 1.0 (right).
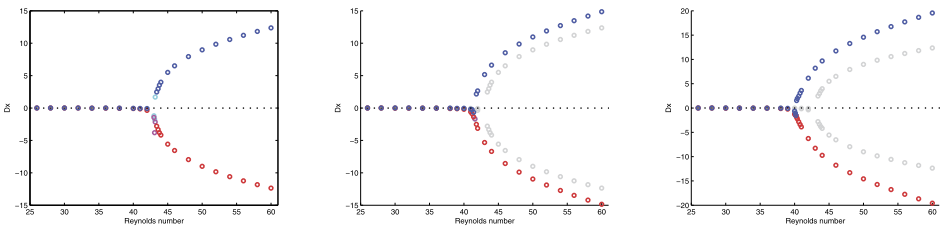

Figure 15: The bifurcation diagram of the sudden expansion flow problem for **ER** $= 3$ with slip parameter $\beta = 0.5$.
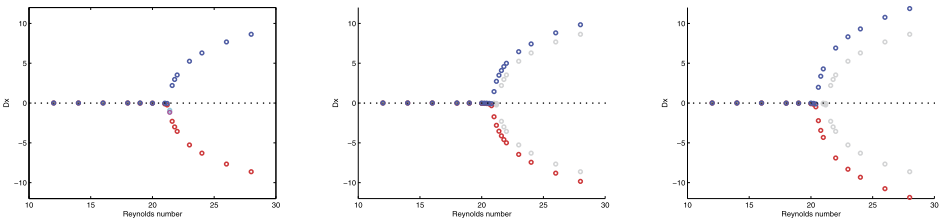

Figure 16: The bifurcation diagram of the sudden expansion flow problem for **ER** $= 5$ with $\beta = 0.0$ (left) 0.5 (middle), and 1.0 (right).

the cases of **ER** $= 2$, 3, and 5, respectively. The bifurcation diagram of **ER** $= 5$ is almost perfect, but the bifurcation diagram of **ER** $= 2$ is still not ideal, especially for the no-slip case. There are many imperfect points.

We summarize the critical Reynolds numbers for a different combination of **ER** and the slip parameter in Table 5. This table indicates that when we increase the slip parameter, the critical Reynolds number decreases.

Table 5: Critical Reynolds number for different slip parameters in different expansion ratio

ER	2	3	5
no slip	127.5	43.1	21.5
$\beta = 0.5$	120.5	41.6	21.0
$\beta = 1.0$	114.3	40.1	20.5

5. Concluding remarks

In this work, we numerically studied how the behavior of an incompressible fluid flow confined within a cavity or through a channel depends on whether the slip boundary conditions are imposed or not. Two benchmark problems, the lid-driven cavity problem and the sudden expansion flow problem, were taken as numerical examples. We employed the pseudo-transient NKS algorithm based on GLS finite element formulation for finding the steady-state lid-driven flow solution and performing the pitchfork bifurcation analysis for the sudden expansion flow problem. For the lid-driven cavity flow, our numerical results showed that the slip boundary condition did not change the global flow structure. For example, the center of the primary vertex remained the same as the values of the slip parameter increased. On the other hand, the slip boundary condition had some local impact on the behavior of flows near the boundary. One additional small eddy was generated near the left bottom corner for a larger value of β. For the sudden expansion flow, we found that the critical Reynolds number for symmetry-breaking bifurcation depends on the slip parameter. The flow system became physically unstable as the value of β increased so that the pitchfork bifurcation occurred at a smaller value of Re.

References

[1] ParaView homepage. http://www.paraview.org/.

[2] CUBIT homepage. https://cubit.sandia.gov/, 2008.

[3] S. Balay, S. Abhyankar, M. Adams, J. Brown, P. Brune, K. Buschelman, L. Dalcin, A. Dener, V. Eijkhout, W. Gropp, et al. PETSc users manual. 2019.

[4] M.P. Brenner E. Lauga and H.A. Stone. In *Microfluidics: The No-Slip Boundary Condition*, chapter 15. J. Foss, C. Tropea and A. Yarin and Springer, 2005.

[5] L.P. Franca and S.L. Frey. Stabilized finite element methods. II: The incompressible Navier-Stokes equations. *Comput. Methods Appl. Mech. Engrg.*, 99:209–233, 1992. MR1186727

[6] Q. He and X.-P. Wang. Numerical study of the effect of Navier slip on the driven cavity flow. *Z. Angew. Math. Mech.*, 68:856–871, 2012. MR2572640

[7] C.-Y. Huang and F.-N. Hwang. Parallel pseudo-transient Newton-Krylov-Schwarz continuation algorithms for bifurcation analysis of incompressible sudden expansion flows. *Appl. Numer. Math.*, 60:738–751, 2010. MR2646473

[8] G. Pineau J.-L. Guermond, C. Migeon and L. Quartapelle. Start-up flows in a three-dimensional rectangular driven cavity of aspect ratio $1 : 1 : 2$ at $Re = 1000$. *J. Fluid Mech.*, 450:169–199, 2002. MR1886212

[9] V. John. Slip with friction and penetration with resistance boundary conditions for the Navier-Stokes equations – numerical tests and aspects of the implementation. *J. Comput. Appl. Math.*, 147:287–300, 2002. MR1933597

[10] V. John and A. Liakos. Time-dependent flow across a step: the slip with friction boundary condition. *Int. J. Numer. Methods Fluids*, 50:713–731, 2006. MR2199095

[11] G. Karypis. METIS web page. http://glaros.dtc.umn.edu/gkhome/metis/parmetis/overview.

[12] A. Kundt and E. Warburg. On friction and thermal conductivity in rarefied gases. *Philosophical Magazine*, 50:53, 1875.

[13] J.C. Maxwell. On the condition to be satisfied by a gas at the surface of a solid body. *Scientific Papers*, 2:704, 1879.

[14] C.L. Navier. Mémoire sur les lois du mouvement des fluides. *Mem. Acad. R. Sci. Paris.*, 6:389–416, 1823.

[15] Y. Saad. *Iterative Methods for Sparse Linear Systems*. SIAM, 2003. MR1990645

Wen-Lieh Hsu
Department of Mathematics
National Central University
Jhongli District
32001, Taoyuan City
Taiwan
E-mail address: hsuweilieh@gmail.com

Feng-Nan Hwang
Department of Mathematics
National Central University
Jhongli District
32001, Taoyuan City
Taiwan
E-mail address: hwangf@math.ncu.edu.tw
URL: http://www.math.ncu.edu.tw/~hwangf